# Pro+: Automated protrusion and critical shear stress estimates from 3D point clouds of gravel beds

E.M. Yager[1*], J. Shim[1], R. A. Hodge[3], A. Monsalve[1], D. Tonina[1], J. P. L. Johnson[2] and L. Telfer[1]

[1] Center for Ecohydraulics Research, Department of Civil and Environmental Engineering, University of Idaho

[2] Department of Geological Sciences, University of Texas at Austin

[3] Department of Geography, Durham University

* eyager@uidaho.edu

## Abstract

The dimensionless critical shear stress ($\tau^*_c$) needed for the onset of sediment motion is important for a range of studies from river restoration projects to landscape evolution calculations. Many studies simply assume a $\tau^*_c$ value within the large range of scatter observed in gravel-bedded rivers because direct field estimates are difficult to obtain. Informed choices of reach-scale $\tau^*_c$ values could instead be obtained from force balance calculations that include particle-scale bed structure and flow conditions. Particle-scale bed structure is also difficult to measure, precluding wide adoption of such force-balance $\tau^*_c$ values. Recent studies have demonstrated that bed grain size distributions (GSD) can be determined from detailed point clouds (e.g., using G3Point open-source software). We build on these point cloud methods to introduce Pro+, software that estimates particle-scale protrusion distributions and $\tau^*_c$ for each grain size and for the entire bed using a force-balance model. We validated G3Point and Pro+ using two laboratory flume experiments with different grain size distributions and bed topographies. Commonly used definitions of protrusion may not produce representative $\tau^*_c$ distributions and Pro+ includes new protrusion definitions to better include flow and bed structure influences on particle mobility. The combined G3Point/Pro+ provided accurate grain size, protrusion, and $\tau^*_c$ distributions with simple GSD calibration. The largest source of error in protrusion and $\tau^*_c$ distributions were from incorrect grain boundaries and grain locations in G3Point and calibration of grain software beyond comparing GSD is likely needed. Pro+ can be coupled with grain identifying software and relatively easily obtainable data to provide informed estimates of $\tau^*_c$. These could replace arbitrary choices of $\tau^*_c$ and potentially improve channel stability and sediment transport estimates.

**Keywords:** point cloud, critical shear stress, protrusion, sediment transport, grain size

## 1. Introduction

Sediment transport can influence channel stability, flooding risks, reservoir lifetimes, and aquatic habitat for threatened and endangered species (Duffin et al., 2023; Garcia, 2008). Bedload transport calculations typically include sediment motion thresholds that must be exceeded before transport begins. The dimensionless critical shear stress (critical Shields stress, $\tau^*_c$) is a commonly used threshold and the critical Shields stress for the median grain size ($\tau^*_{c50}$) may be approximately uniform in lower-gradient gravel bedded rivers that experience hydraulically rough flow (Buffington and Montgomery, 1997; Shields, 1936). Despite this constant average value, substantial scatter exists between different gravel bed rivers in both $\tau^*_{c50}$ (e.g., 0.01-0.1) and the critical Shields stress ($\tau^*_{ci}$) for a given grain size on the bed ($D_i$). Recent studies show that $\tau^*_{c50}$ can also temporally vary within a river, further complicating the choice of a representative value (Charru et al., 2004; Haynes and Pender, 2007; Johnson, 2016; Masteller et al., 2019; Ockelford et al., 2019; Pretzlav et al., 2020; Rickenmann, 2020; Turowski et al., 2011). No generally applicable method exists to select a specific $\tau^*_{c50}$ value in space and time within the scatter of observed values.

Variations in $\tau^*_c$ are attributed to methodological (# 1-2) and physical differences (# 3-5) in: 1) onset of motion definitions, 2) sediment transport measurement techniques, 3) bed grain size distributions (GSD) including armoring, 4) flow characteristics (e.g. velocity profiles), and 5) bed structure (Bathurst, 2013; Buffington et al., 1992; Buffington and Montgomery, 1997; Hodge et al., 2013; Lamb et al., 2008, 2017a; Ockelford and Haynes, 2013; Recking, 2009; Schmeeckle et al., 2007; Shvidchenko et al., 2001; Voepel et al., 2019; Wiberg and Smith, 1987; Yager et al., 2012, 2018a). Temporal variations in $\tau^*_c$ are not a methodological artefact because the same definition and method of estimating the onset of motion are usually employed in an individual channel/experiment over time. Consequently, the last three physical differences are the most mechanistically important to consider for both spatial and temporal variations in $\tau^*_c$. Observed temporal variations in $\tau^*_c$ without significant bed GSD alterations further implies that near-bed flow hydraulic or bed structural changes alone could be responsible in some streams (Masteller et al., 2019). In theory, bed structure could also adjust faster than bed GSD in response to changes in flow or sediment supply over time.

Protrusion and intergranular friction are key components of bed structure that influence $\tau^*_c$ (Bi et al., 2011; Cúñez et al., 2022; Fenton and Abbott, 1977; Hodge et al., 2020; Luo et al., 2023; Masteller and Finnegan, 2017; Yager et al., 2018a). Intergranular friction can empirically include the effects of particle imbrication, orientation, angularity, cohesion, interlocking, clustering, and porosity. Protrusion, which is often defined as the distance a particle extends above the surrounding mean bed elevation, varies with relative particle size (Hodge et al., 2020; Kirchner et al., 1990; Smith et al., 2023). Protrusion exerts strong controls on the applied fluid forces on a particle by altering the grain area exposed to the flow as well as the pressure distribution around the grain (Schmeeckle et al., 2007). Particles with greater protrusion typically have higher drag forces but possibly lower lift forces (Schmeeckle et al., 2007). Conversely, resisting forces impeding motion decline as particle protrusion increases because higher protruding particles are less buried by surrounding sediment (Sanguinito and Johnson, 2012; Yager et al., 2018a). The net result of these driving and resisting forces is that higher protrusion lowers $\tau^*_c$ to make particles easier to move. In theory, $\tau^*_c$ can decrease by orders of magnitude as particle protrusion changes from a completely buried grain to one that is fully exposed (Hodge et al., 2020; Yager et al., 2018a).

Despite its importance, protrusion is not widely used to estimate $\tau^*_c$ because of two major limitations. First, protrusion needs to be combined with validated force balance models to estimate $\tau^*_c$, which could be addressed by testing published force balance models but few suitable datasets exist (Kirchner et al., 1990; Lamb et al., 2008; Voepel et al., 2019; Wiberg and Smith, 1987; Yager et al., 2018a). Second, protrusion is not easily measured in the field or laboratory flume. It is often manually measured using a ruler or point gauge, which is subject to potentially large errors and subjective measurement location choices (Kirchner et al., 1990;

Yager et al., 2018a). Any manual measurement of protrusion is also extremely time consuming and could disturb the bed. Protrusion has been estimated from high-resolution point clouds or 3D bed topographies (Hodge et al., 2020), which removes some measurement uncertainties and has lower bed disturbance potential. But such measurements still require identification of grain boundaries, which is often done manually (Hodge et al., 2013).

In addition to these limitations, the protrusion definition that, when used in force balance equations, provides the most representative $\tau^*_c$ value is also uncertain. Protrusion is often divided into exposure and projection, which are defined as the distances a grain extends above a locally high bed elevation and the local surrounding mean bed elevation, respectively (Buffington et al., 1992; Kirchner et al., 1990). In theory, exposure accounts for particle sheltering from the flow by upstream obstructions whereas projection incorporates the effects of a velocity profile on particle motion. The locations included in the estimate of mean surrounding bed elevation vary between studies and have included: a 1-D transect upstream and downstream of the particle (Buffington et al., 1992; Kirchner et al., 1990), only elevations immediately downstream (Yager et al., 2018a), only elevations in a 1-D transect upstream (Smith et al., 2023), 2D areas upstream and downstream (Hodge et al., 2013), and 2D areas from different potential flow angles of attack (Hodge et al., 2020; Voepel et al., 2019). For the locally high bed elevation, the maximum upstream elevation in a 1-D transect (Buffington et al., 1992; Kirchner et al., 1990), the 95$^{th}$ percentile of upstream elevations in a 1-D transect (Hodge and Buechel, 2022), and the exposed area from complex 3D topography at various angles of attack have all been employed (Hodge et al., 2020; Voepel et al., 2019). Almost all surrounding bed elevations for protrusion estimates are within a distance equivalent to $D_{84}$ (84$^{th}$ percentile of bed GSD) from the particle. This assumes that the downstream sheltering distance of an obstruction is similar to the bed roughness length, which is often represented by the $D_{84}$. However, a distance of 8-10 obstacle heights downstream of an obstruction may be needed for the flow to return to unobstructed values rather than just over one $D_{84}$ (Heald et al., 2004; Schmeeckle and Nelson, 2003). In addition, for grains smaller than the $D_{50}$, protrusion may differ if calculated using immediately upstream elevations vs. elevations averaged as far as $10D_{50}$ upstream (Smith et al., 2023).

To address these limitations in measuring protrusion and subsequent uncertainties in calculated $\tau^*_c$, we propose a new objective, fast, and automated method (Pro+) of obtaining protrusion and $\tau^*_c$ from point clouds or DEMs. Pro+ requires the bed topography in the format of a detrended (local streamwise bed slope removed) bed point cloud, the diameter of each grain, and either the perimeter of each grain or the portion of the point cloud corresponding to each grain (hereinafter called grain point cloud). The grain diameters and grain perimeters/point clouds can be obtained from a range of techniques such as deep learning or grain detection in point clouds (Butler et al., 2001; Chen et al., 2020; Steer et al., 2022; Walicka et al., 2021; Wu et al., 2021). For example, the software G3Point automates grain size measurements from 3D point clouds using flow routing algorithms and ellipsoidal fits to grains (Steer et al., 2022). We develop Pro+ using inputs from either G3Point or algorithms that output grain perimeters and grain sizes. Pro+ uses particle perimeters to determine the protrusion for each grain and calculates $\tau^*_c$ distributions for each grain size bin and the entire bed using a previously published force balance model (Yager et al., 2018a).

We validate G3Point and Pro+ using manually estimated grain sizes and grain perimeters from orthomosaics of two laboratory experiments with different grain size distributions and bed topographies. We substitute the manually measured grain perimeters and sizes into the Pro+ code to calculate protrusion and $\tau^*_c$ distributions. We compare these grain size, protrusion, and $\tau^*_c$ values to the fully automated values produced by the combination of G3Point/Pro+. Using Pro+, we also explore how protrusion distributions are influenced by the: 1) distance over which surrounding bed elevations are measured, 2) representative surrounding bed elevation (e.g., median, maximum) used to define protrusion, and 3) direction (upstream or downstream of particle) of surrounding elevations. We use this information to refine protrusion calculations and the force balance model in Pro+.

## 2. Methods

Our method section outlines 1) $\tau^*_c$ calculations and inputs as well as the associated protrusion definitions used in Pro+, 2) details of the automated protrusion measurements in Pro+, 3) two laboratory experiments, 4) manual measurements from the experiments, 5) testing Pro+ assumptions using manual measurements, and 6) validating Pro+/G3Point using manual measurements. Steer et al. (2022) provides details on G3Point calculations including point cloud detrending (details provided in G3Point code), flow routing to initially define possible grain locations, algorithms to merge grains, and ellipsoidal fits to obtain grain sizes and grain point clouds.

### 2.1 Pro+ automated $\tau^*_c$ estimates

In Pro+ we employ the force balance equations of Yager et al. (2018a) because they represent the influence of bed structure on both applied fluid forces and resisting bed forces (see supporting information for full equations). The force balance requires grain size and protrusion. To measure protrusion, Pro+ needs inputs from either: 1) G3Point, which provides the point cloud associated with each grain (grain point cloud) and grain size, or 2) other software (see introduction) that provides grain perimeter coordinates and grain sizes. If using G3Point, Pro+ only employs grains that are well fit by ellipsoids according to G3Point standards (Steer et al., 2022). The intermediate grain axis ($b$) represents grain size in Pro+ because the force balance equations were derived assuming spherical grains. These equations calculate grain areas exposed to the flow and buried grain volumes that are not easily determined for ellipsoidal shapes. Almost all force balance equations for the onset of sediment motion make similar assumptions of spherical particle shapes (Buffington et al., 1992; Hodge et al., 2013; Hodge and Buechel, 2022; Kirchner et al., 1990; Lamb et al., 2008; Wiberg and Smith, 1987).

We alter the equations of Yager et al. (2018a) to use two different protrusion definitions, one protrusion ($p_D$) that affects driving fluid forces and one ($p_R$) that affects forces resisting particle motion. Both $p_D$ and $p_R$ are the difference between the highest elevation on a particle and a representative surrounding bed elevation, which differs between $p_R$ and $p_D$. Pro+ determines $p_R$ using the median surrounding bed elevation. Calculated resisting forces depend on $p_R$ because of the 1) overburden weight caused by partial or full particle burial (i.e., burial=$b$-$p_R$), and 2) associated intergranular friction of the particle sliding past any burying grains. We assume that burial effects are likely caused by grains that occur at relatively high (average or greater) elevations surrounding the particle of interest to define $p_R$.

In contrast, we calculate $p_D$ based on a low ($10^{th}$) percentile of the surrounding bed elevations because of how flow velocities are calculated in Pro+. Instead of assuming a logarithmic velocity profile as in Yager et al. (2018a), we use a hybrid mixing-length velocity profile equation that was specifically developed for the near-bed roughness layer (Lamb et al., 2017b). This equation provides a better estimate of the flow velocity ($u$) within the roughness layer and calculates the same $u$ as that estimated by the logarithmic profile for vertical distances from the bed ($z$) that are much greater than the roughness length ($k_s$). We use the simplified version of the velocity profile equation for an impermeable bed (equation 11 in Lamb et al. (2017b)) in which $u$=0 when $z$=0. For $p_D$ estimates, $z$=0 should correspond to a low percentile of the surrounding bed elevation to allow the calculated $u$ to be nonzero through most of the roughness layer. Details on Pro+ extraction of surrounding bed elevations are provided in the next section.

In the velocity profile equation, $k_s$ is often assumed to be a function of $D_{84}$ but the standard deviation of bed elevations ($\sigma_z$) could be more representative because it allows for the influence of other roughness sources beyond grains (Aberle and Smart, 2003; Bertin et al., 2017; Ferguson et al., 2019; Johnson, 2014, 2017; Powell et al., 2016; Schneider et al., 2015; Smart et al., 2002; Yochum et al., 2012). Given the uncertainties in $k_s$ definition, Pro+ has three choices available for $k_s$: 1) a user specified value, 2) Pro+ calculated $D_{84}$ from the input GSD, or 3) Pro+ calculated $\sigma_z$ from the input detrended bed point cloud.

Finally, pivot ($\phi_p$) and intergranular friction angles ($\phi_f$) are used in the force balance equations but are difficult to directly measure and are therefore assumed in Pro+. Either a single value or a normal distribution of $\phi_f$ can be used; the mean, standard deviation, and number of random samples of the distribution are required inputs. Pro+ can either effectively neglect pivot angle effects (see supporting information for details) or can use a $\phi_p$ distribution, which is obtained from equation (4) in Kirchner et al. (1990). This equation has considerable uncertainties and may only be valid for certain percentiles of the distribution (see Kirchner et al. (1990) for details). In addition, one study found that $\phi_p$ may not exert a strong mechanistic control on $\tau_c^*$ (Hodge et al., 2020).

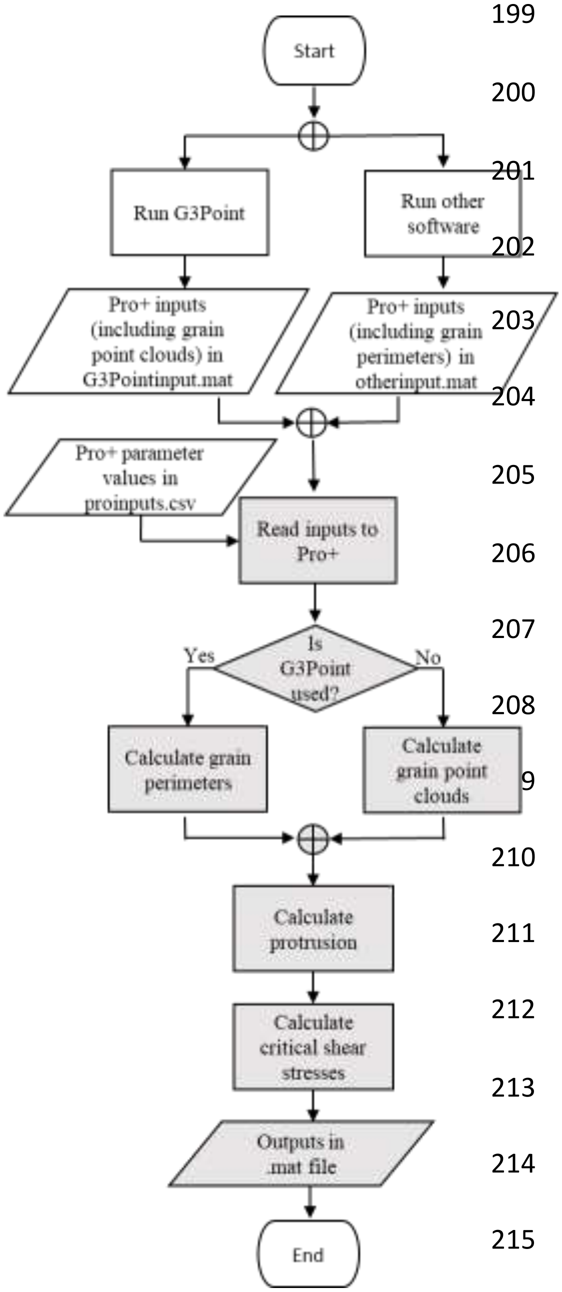


Figure 1. Flow chart of the necessary calculations and inputs before (white) running Pro+ and a broad overview of calculations within Pro+ (grey).

In summary, Pro+ calculations of $\tau^*_c$ employ assumed constants (e.g., drag coefficients), $\phi_p$, $\phi_f$, and $k_s$ values as well as measurements of $b$, $p_D$, $p_R$, for each grain on the bed. A complete list of input requirements for Pro+ is provided in the supporting information. If a single value of $\phi_f$ and no $\phi_p$ is used, then Pro+ will obtain a single value of $\tau^*_c$ for each particle. If distributions of $\phi_f$ and $\phi_p$ are used, then each individual grain will have a distribution of potential $\tau^*_c$ values because of these assumed angle distributions (see Yager et al., 2018a for details). Pro+ combines all $p_D$, $p_R$, and $\tau^*_c$ values for particles within each grain size bin to determine the distribution of $p_D$, $p_R$, and $\tau^*_{ci}$ for each representative grain size. Such $\tau^*_{ci}$ values for each grain size could be used to create hiding functions. All available $p_D$, $p_R$, and $\tau^*_c$ are also combined to obtain these distributions for the entire bed. Application of these full $\tau^*_{ci}$ distributions, or single representative values of each $\tau^*_{ci}$ distribution, in bedload transport predictions is examined in the discussion section.

### 2.2 Pro+ automated protrusion estimates

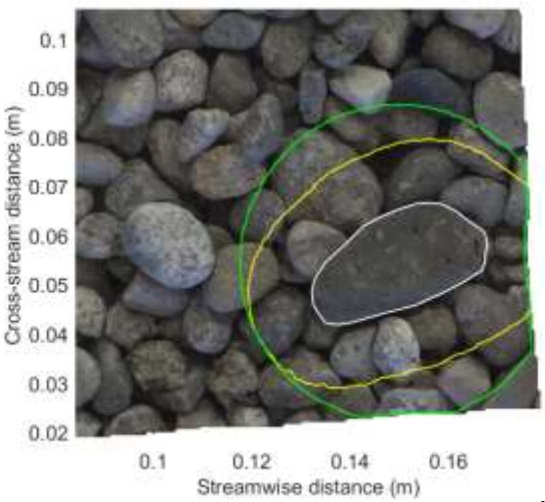


Figure 2. Example surrounding bed area used to calculate protrusion for one grain. The grain perimeter shape is shown in white, and the farthest extent of the irregular and circular shaped searches are shown in yellow and green, respectively, for an example search distance of 0.013 m. Points are included in the surrounding bed area if they are between the white grain perimeter and the respective colored line.

We now outline the details of Pro+ calculations of protrusion ($p_D$ and $p_R$), which require the point cloud associated with each grain (grain point cloud) and the grain perimeters in *x* and *y* coordinates (streamwise and cross-stream). A high-resolution DEM could also be employed for this analysis if the DEM is converted to a point cloud format, which is required in both the G3Point and Pro+ codes. The two potential software inputs (G3Point or other software) to Pro+ either provide the grain point cloud or the grain perimeter and therefore Pro+ calculations differ slightly depending on the pre-run software (Figure 1). If using G3Point to input individual grain point clouds, Pro+ calculates the perimeter of each particle as the outer planform boundary of the provided particle point cloud. This allows for irregular grain perimeters that closely track the actual grain shape (Figure 2). If grain perimeters are instead input from other software, Pro+ determines the point cloud of each grain using these perimeters and the provided detrended bed point cloud.

The remaining calculations are the same regardless of the pre-run software inputs to Pro+ (Figure 1). Pro+ determines the maximum elevation of every particle from each particle point cloud. A horizontal search distance must be input for Pro+ to identify the surrounding bed elevations around each particle. Similar to $k_s$, the search distance should be partly informed by the expected sheltering distance from surrounding obstacles. Force chains, which mechanistically influence resisting forces and are composed of structures of grains that are held together by large forces, can also extend considerable distances from particles (Bi et al., 2011; Daniels et al., 2017). The Pro+ options for defining the search distance are therefore the same as those for $k_s$: a user specified value, $D_{84}$, or $\sigma_z$. The surrounding bed elevations include all points within the bed point cloud that are within the search distance, which starts at the grain perimeter. The irregularly shaped surrounding bed area closely mimics the grain shape (Figure 2). We included all elevations within this bed area rather than just those only upstream or downstream of the grain because of the potential importance of 1) different flow directions on driving forces, and 2) all locations around the particle in controlling resisting forces (Hodge et al., 2020; Voepel et al., 2019; Yager et al., 2018a). The $10^{th}$ and $50^{th}$ percentiles of the surrounding bed elevations are subtracted from the maximum grain elevation to determine $p_D$ and $p_R$, respectively. We evaluate various assumptions in the protrusion calculations using data collected in laboratory experiments (see next three sections).

### 2.3 Laboratory experiments

To test assumptions in Pro+ and to validate Pro+ and G3Point outputs, we conducted two experiments in the Center for Ecohydraulics Research (CER) Mountain Streamlab, which is a 20 m long and 2 m wide flume with an adjustable slope that was set to 1.15% (Budwig and Goodwin, 2012). In both experiments, a bulk sediment mixture consisted of 10% 0.5 mm sand and 90% gravel with a $D_{50}$ of 11 mm. Further details on the sand and gravel particle shapes are provided in Yager et al. (2018). We varied the gravel sorting parameter ($\sigma_g=(D_{84}/D_{16})^{0.5}$ where $D_{16}$ is the 16th percentile of the gravel distribution) of the bulk gravel mixture between experiments to create a narrow ($\sigma_g$=1.23) or wide ($\sigma_g$=2.71) bulk gravel size distribution that can influence particle protrusion (Kirchner et al., 1990; Smith et al., 2023). The narrow GSD experiment had a bulk mixture $D_{16}$, $D_{84}$, and $D_{max}$ (maximum size) of 9, 14, and 31 mm, respectively, whereas the wide GSD bulk mixture had values of 4, 30, and 63 mm, respectively.

The narrow GSD experiment was not water-worked, whereas the wide GSD experiment was water worked without any upstream sediment supply to create a well-developed armor layer. The experiments were not scaled to a specific protype and we used different GSD and bed preparation techniques (screeded vs. water working) to vary potential particle arrangements and bed topographies (Masteller and Finnegan, 2017; Ockelford and Haynes, 2013), which could affect GSD accuracy from G3Point and protrusion accuracy from Pro+. An adjustable tailgate at the end of the flume ensured uniform flow during water working, which was validated with flow depth measurements throughout the flume length. Water working consisted of a 12-hour long flow at a constant discharge of 0.7 $m^3$/s that visibly moved the bulk mixture $D_{84}$ in preliminary experiments. This was followed by a 4-hour long flow (0.5 $m^3$/s) that visibly moved the bulk mixture $D_{50}$ in preliminary experiments and preferentially transported fine sediment into the bed or out of the flume. Similar sequences of flows have armored beds in previous laboratory experiments (Curran and Waters, 2014). We spray painted the armor layer in a 1 m long by 1.5 m wide area, removed all spray-painted grains, and sieved these grains at half-phi intervals. The armor layer $D_{16}$, $D_{50}$, and $D_{84}$ for the wide GSD experiment were 8, 18, and 32 mm (resulting in $\sigma_g$=1.95) with less than one percent sand. We only focus on gravel sized particles because G3Point cannot accurately quantify sand (see Steer et al., 2022).

In the narrow and wide GSD experiments, we photographed the bed surface after placing the bulk sediment mixture in the flume or after water working, respectively. A high-resolution camera (Blackfly 5Mpix; focal length of 12.5 mm; ~20 cm from bed; ~0.05 mm/pix) photographed many (156 in wide GSD or 195 in narrow GSD) images with at least 60% overlap from various angles relative to the bed and around the area of interest (15 m downstream of flume entrance). Each set of photographs contained a carpenter's square that provided scale bars in multiple directions needed for scaling the topography. The photos were used in Structure from Motion photogrammetry (SfM) analyses (Agisoft Metashape professional version 1.5.1) to create scaled point clouds for G3Point/Pro+ measurements and scaled orthomosaics for manual measurements. The original point clouds had an average resolution finer than 0.2 mm (Figure 3) that was decimated to a resolution of 0.4 mm, which enabled use in G3Point (see Steer et al., 2022 for limitations on point cloud size) and facilitated faster calculations in Pro+.

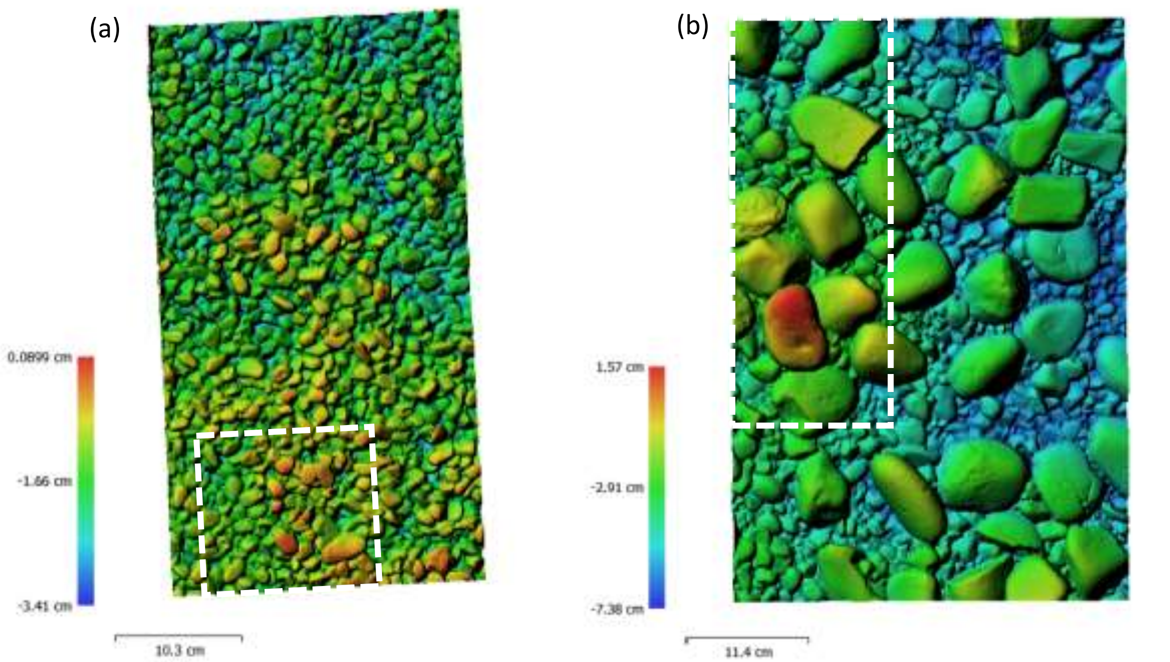


Figure 3. DEMs of the (a) narrow GSD experiment without water working and (b) wide GSD experiment after water working. White dashed boxes outline the areas in each experiment used in the G3Point/Pro+ validation and contained (a) 181 and (b) 302 manually measured grains.

## 2.4 Grain measurements

We needed independent estimates of grain size, protrusion, and $\tau^*_c$ to validate G3Point/Pro+ but different measurement techniques can produce values that are not always directly comparable (Hodge et al., in review). For example, sieved bulk bed samples, pebble counts, and photogrammetry can provide differing GSD because of spatial variability in sample locations and methodological differences/errors. Protrusion from rulers or point gages, computerized tomography (CT) scans, and Pro+ could also differ because of inconsistent sampling of surrounding bed elevations (Hodge et al., in review). Finally, estimated $\tau^*_c$ are known to vary with measurement method (e.g., bedload samples, tracers) and onset of motion definition (Buffington and Montgomery, 1997). To use the same (or similar) techniques/definitions between our validation measurements and G3Point/Pro+, we manually identified and measured grains in the orthomosaic images.

To keep the number of manually digitized grains manageable, we subsampled the point clouds and corresponding orthomosaics to smaller representative areas (0.12 x 0.14 m vs. 0.15 x 0.35 m for narrow vs. wide GSD experiments) (Figure 3). Different shaped areas were used because of the different grain sizes and orientations between the two experiments; capturing the largest grains in the wide GSD experiment required using a more rectangular area that mimicked the orientation of these particles. For a given experiment, these smaller areas had the same $\sigma_z$ as the entire bed shown in Figure 3 and were therefore topographically representative. We manually measured the visible *b* axis and digitized the perimeter of every grain visible in the orthomosaic images, which resulted in 181 and 302 measured grains for the narrow and wide GSD experiments, respectively. Therefore, the chosen areas also provided a sample size large enough to determine the GSD. We substituted the manually measured perimeters in the Pro+ code in place of the G3Point/Pro+ perimeters to calculate 'manual-based' $p_D$ and $p_R$ values and evaluate Pro+ assumptions (Section 2.5). We also used these manual perimeters and grain sizes in the Pro+ code to determine how grain identification errors in G3Point propagated to errors in G3Point/Pro+ estimated grain size, protrusion, and $\tau^*_c$ values (Section 2.6).

### 2.5 Testing Pro+ assumptions

Before validating Pro+, we needed to test several assumptions and calculation methods. For all calculations in this section, we used the manual measurements in the wide GSD experiment as an example. Pro+ uses two different representative surrounding bed elevations (10$^{th}$ and 50$^{th}$

percentiles, $p_D$ and $p_R$) to define protrusion. But in previous studies (see Introduction), the representative bed elevation(s) is usually: 1) only the median or average, 2) only a high percentile (e.g., 84$^{th}$ or 90$^{th}$), or 3) a combination of the median or mean (projection) and a high percentile (exposure). We therefore calculated protrusion using the 10$^{th}$ ($p_D$), 50$^{th}$ ($p_R$), and 84$^{th}$ (no associated Pro+ protrusion variable) percentiles of the surrounding bed elevations to determine how they affect protrusion distributions.

We also investigated the influence of the surrounding bed search area shape, search distance, and search location. Our irregularly shaped search area can be computationally expensive and we therefore tested a more efficient simple circular search distance that starts at the grain centroid (Figure 2). To enable comparison with the irregularly shaped search that starts at the grain perimeter, the actual search distance for the circular shape was the grain *b* axis plus the specified search distance magnitude. Similar to the irregularly shaped search, the circular search also excludes any points occupied by the grain of interest. We investigated the influence of these two different search shapes (irregular vs. circular) on $p_D$ and $p_R$ distributions for a range of specified search distances. Finally, previous protrusion estimates (see Introduction) use different surrounding bed locations (upstream, downstream, all) relative to the grain of interest. We therefore evaluated using only points in the surrounding bed search that were upstream or downstream of a flow perpendicular line through the grain centroid to calculate $p_D$ and $p_R$ distributions. Both upstream and downstream areas extended along the grain sides to the grain centroid.

### 2.6 Validating G3Point and Pro+

After testing assumptions in Pro+, we then used the manual-based $b$, $p_D$ and $p_R$ distributions from both experiments to validate G3Point/Pro+. We substituted these manual-based $b$, $p_D$, and $p_R$ distributions into the $\tau^*_c$ calculations in Pro+ to obtain $\tau^*_c$ distributions, which are hereinafter also called "manual-based" $\tau^*_c$ values for simplicity. Given that differences in dimensional critical shear stresses ($\tau_c$) are intuitively easier to compare than dimensionless values, we convert all $\tau^*_c$ values to $\tau_c$ using Shields equation.

To compare G3Point/Pro+ outputs with these manual-based $b$, $p_D$, $p_R$, and $\tau_c$ distributions, we first "calibrated" tunable G3Point input variables using the trial-and-error approach of Steer et al. (2022) on the subsampled point clouds (Figure 3). Most researchers lack manually estimated grain perimeters and therefore manual-based protrusion and $\tau_c$ estimates for explicit Pro+ testing/calibration. We therefore focused only on G3Point calibration using measured GSD and grains visible in orthomosaics. We adjusted several G3Point inputs to provide: 1) reasonably accurate fits to manual GSDs (Steer et al., 2022) and 2) the most visually comparable grain perimeters to those on the orthomosaics. These adjustable input variables were the minimum number of points that should contain a grain ($n_{min}$), scaling factor to determine grain merging ($C_F$), two different angles (between the normals of grain crest points) below which two grains are merged ($\alpha$, $\beta$), and threshold flatness below which to remove a grain ($\phi_{flat}$). We then fixed these input variables for a given experiment and explored a range of G3Point $k$ values, which is the number of nearest neighbors for the flow routing algorithm and strongly controls G3Point accuracy (Steer et al., 2022).

Goodness of fit between the G3Point and manual GSD was determined using p values from a two-sample Kolmogorov-Smirnov test ($\alpha$=0.05) and percent errors in certain GSD percentiles.

For a range of $k$ values, we highlight results from the G3Point input variable combination that produced high p values and low percent errors for GSD in each experiment. Percent errors in the $10^{th}$, $50^{th}$, and $90^{th}$ GSD percentiles were the absolute value of the difference between the manual and G3Point estimate divided by the manual estimate. We also calculated p values and percent errors for protrusion and $\tau_c$ distributions using a range of $k$ values and the optimal G3Point input variable combination in each experiment.

The direct ellipsoid fitting method in G3Point did not perform well in our experiments and we only discuss the inertial fitting method. The default G3Point methodology of removing minima from the point cloud caused many grains in locally flat areas to be misidentified and we did not remove minima in our calculations. Further details on ellipsoid fitting methods and G3Point input variables are provided in Steer et al. (2022).

To calculate protrusion, we used the irregular search shape (Figure 2) with an example search distance of 0.014 m in both our manual-based and G3Point/Pro+ validation calculations. The search distance needed to accurately define protrusion is still an open question in the literature (Smith et al., 2023) and as discussed above, is likely related to the $D_{84}$ or $\sigma_z$. For the narrow GSD experiment, the search distance of 0.014 m equaled the bulk mixture $D_{84}$ and was far greater than the $\sigma_z$ of 0.004 m. In the wide GSD experiment, our search distance equaled $\sigma_z$. We could not use a search distance that equaled the $D_{84}$ (0.032 m) of the wide GSD experiment because 0.032 m was larger than the $x$ dimension of our test area (Figure 3). In both the G3Point/Pro+ and manual-based $\tau_c$ validation estimates, we used: $k_s$=$\sigma_z$ of the detrended point cloud in each experiment, $\phi_f$ set to 60°, and no $\phi_p$. Preliminary tests showed that using distributions of $\phi_f$ and $\phi_p$

artificially inflated the $\tau_c$ sample size in statistical comparisons compared to using single values of these angles.

## 3. Results

We first use the manual-based protrusion estimates to investigate protrusion sensitivity to the representative surrounding bed elevation, search shape, search distance, and search location (Section 3.1). We then test G3Point/Pro+ $b$, $p_R$, $p_D$, and $\tau_c$ distributions against the manual-based distributions in both experiments (Sections 3.2 and 3.3).

### 3.1 Protrusion sensitivity

We use the manual-based protrusion distributions for the wide GSD experiment as representative examples to test protrusion sensitivity. We first examine sensitivity of the $p_R$ and $p_D$ distributions in each grain size bin to the search shape and search distance (varied between 2-16 mm). For simplicity, we report medians of the $p_R$ and $p_D$ distributions in example end member (2 and 55 mm) and intermediate (7 and 19 mm) grain size bins. For a given search distance and grain size, the circular search shape systematically under-estimated median $p_R$ and often over-estimated median $p_D$ compared to the irregular search shape (Figure 4c and 4d) that mimicked the shape of the grain. The underestimation of median $p_R$ by the circular search shape also increased with

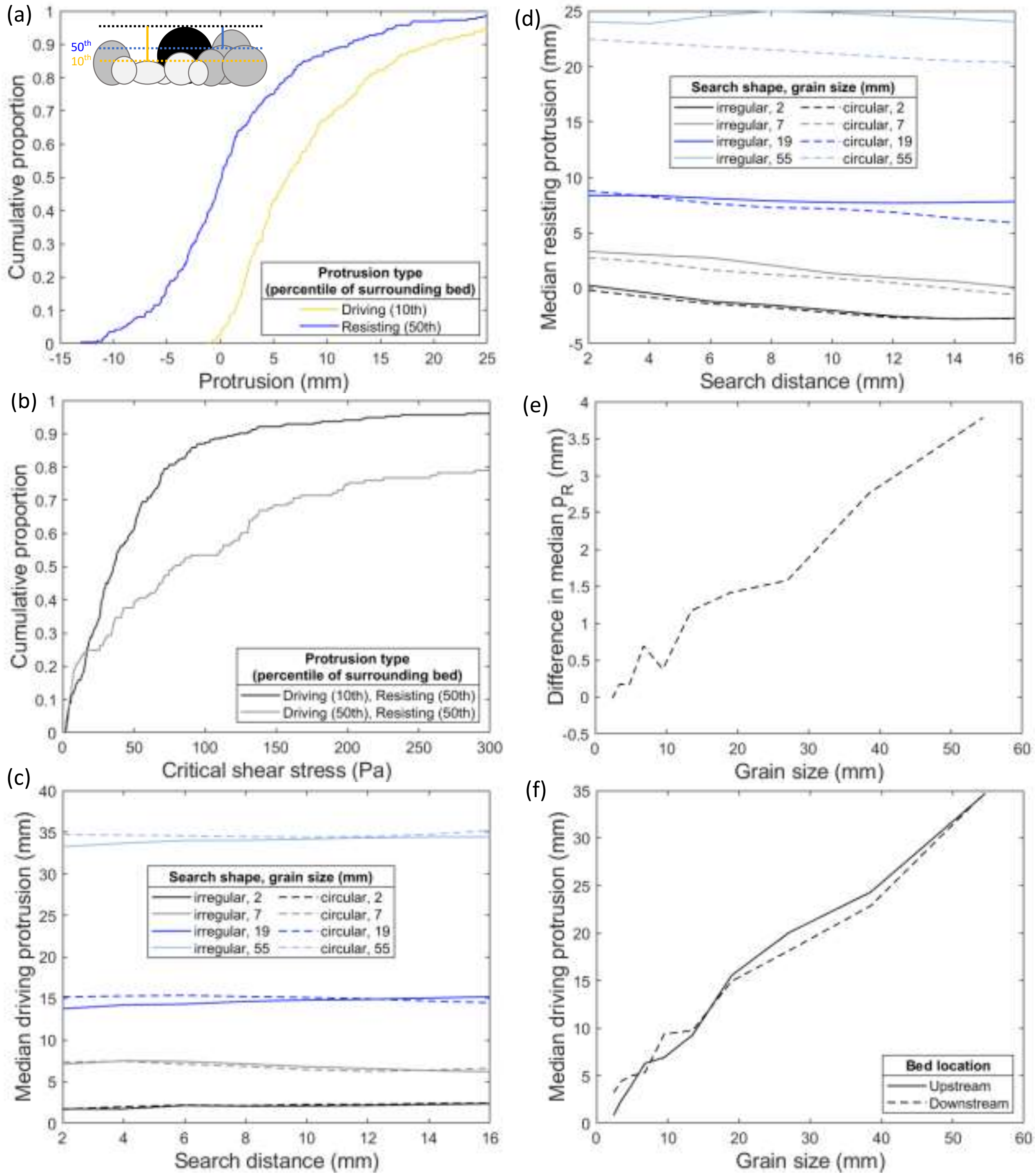


Figure 4. Sensitivity of manually measured protrusion values for the wide GSD experiment. (a) Protrusion distributions for all grains using an irregular search shape and the 10th (driving protrusion, $p_D$) and 50th (resisting protrusion, $p_R$) percentiles of the surrounding bed elevation. Inset cartoon shows example $p_R$ (blue line) and $p_D$ (yellow line) for the black grain. All grains below the local (grain and search radius dependent) 50th percentile bed elevation would have negative $p_R$ and are shown in light gray. (b) Calculated critical shear stresses for all grains using $p_R$ and $p_D$ from (a) or by replacing $p_D$ for $p_R$ in all calculations. (c) Median $p_D$ and (d) median $p_R$ as functions of search distance and search shape (different line types) for example grain sizes (line colors, labeled with average grain size in bin). (e) The difference between the median $p_R$ calculated using an irregular search shape and the median $p_R$ calculated using a circular search shape for each grain size bin. (f) Influence of upstream and downstream search location on median $p_D$ for each grain size bin using an irregular search shape. (a-b) and (e-f) use a search distance of 0.014 m.

greater particle size (Figure 4e). The circular search shape could therefore cause systematic biases in calculated $\tau_{ci}$ changes with grain size. We concluded that such biases outweighed potential efficiency benefits and this shape is not included in Pro+ or in our remaining analyses.

For the irregular search shape, median $p_R$ and $p_D$ for most grain sizes were relatively constant with search distance (Figure 4c and 4d). Two exceptions were that a greater search distance caused median $p_R$ to decrease for smaller grains (e.g., 2 and 7 mm in Figure 4d) and median $p_D$ to slightly increase for larger grains (e.g., 19 and 55 mm in Figure 4c). Given the relative insensitivity of protrusion to search distance, we used a search distance of 0.014 m (see Methods) in all subsequent calculations. We also investigated the role of search location because many studies use different locations (e.g., upstream, downstream, all) of surrounding bed elevations to calculate protrusion. As an example, we show the median $p_D$ for each grain size bin calculated using only upstream or downstream locations. Median $p_D$ was not systematically greater when using either the upstream or downstream locations (Figure 4f). Differences in median $p_D$ between upstream and downstream locations also did not systematically change with grain size. Regardless of employed location, the median $p_D$ increased with coarser grain sizes as expected (Kirchner et al., 1990; Smith et al., 2023). We conclude that using the entire search area is appropriate given that upstream and downstream protrusion values did not display any systematic differences in our analyses.

We finally assessed the impact of the representative surrounding bed elevation on protrusion. The 50$^{th}$ percentile of the surrounding bed elevation is commonly used (see Introduction) but produced a protrusion distribution ($p_R$) in which nearly half of the values were negative (Figure 4a). A higher representative surrounding bed elevation (e.g., 84$^{th}$ percentile) caused even more negative protrusion values (not shown). Negative values of $p_R$ still have calculated resisting forces because they result in a fully buried grain ($p_R$<0 reverts to $p_R$=0 in Pro+ calculations). However, grains with negative protrusions do not have calculated exposed areas to flow, experience zero calculated flow velocities when using velocity profile equations, and have zero calculated lift and drag forces. Therefore, the common methodology of using the 50th percentile (or higher) of the surrounding bed elevation in driving force calculations would result in a large proportion of grains (see cartoon in Figure 4a) without a calculated $\tau_c$ value. The reference bed elevation where $u(z)$=0 for $p_D$ should instead be a low percentile of the distribution that allows for most grains to have calculated velocities, exposed areas, driving forces, and $\tau_c$ values. The 10th percentile of the surrounding bed elevation produced a low percentage of negative protrusions ($p_D$) (Figure 4a), which allowed us to calculate driving forces and $\tau_c$ for most grains. For example, replacing $p_D$ with $p_R$ in calculations of $\tau_c$ for the wide GSD experiment resulted in only 133 grains having an estimated $\tau_c$ instead of 253 grains when using both $p_D$ and $p_R$. Only using $p_R$ also caused systematically larger $\tau_c$ values than if both $p_D$ and $p_R$ were used (Figure 4b).

### 3.2 G3Point validation

To assess G3Point accuracy, we now compare the G3Point and manual GSD in each experiment and compare G3Point grain perimeters to grains visible in the orthomosaics. We discuss the optimal G3Point input variable combination in each experiment (see Table 1) for a range of possible input G3Point $k$ values (see Methods). In each experiment, G3Point produced a GSD (Figure 5a and 5d) that closely resembled the shape of the manually estimated distribution for most tested $k$ values. Certain $k$ values also produced generally low GSD percent errors (Table 1; less than ~15%) in each experiment. These $k$ values mostly produced relatively high GSD p (e.g., p>0.05) values, which implies that G3Point GSD and manual GSD may not be statistically different within the uncertainties of the distributions. Some optimal G3Point input variables were

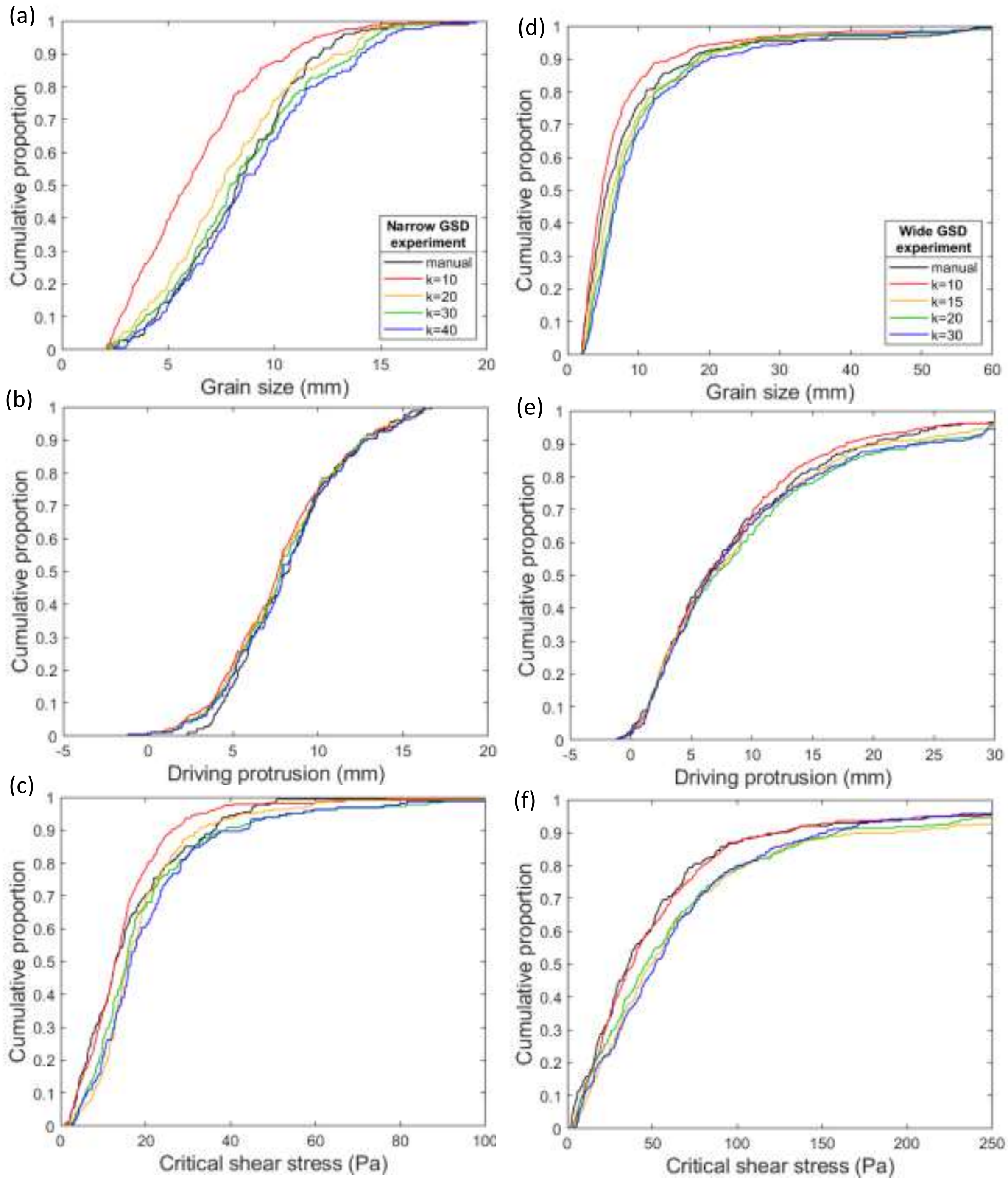


Figure 5. Comparison of manual-based (black lines) and G3Point/Pro+ (colored lines labeled with G3Point *k* value) values for the (left column) narrow GSD experiment and (right column) wide GSD experiment. Each panel shows (a, d) grain size, (b, e) driving protrusion, and (c, f) critical shear stress distributions. Legends in the top figure panels apply for the rest of each column. G3Point/Pro+ distributions are shown for the G3Point input variable combination (provided in Table 1) that optimized G3Point GSD and grain perimeter accuracy.

the same between experiments ($C_F$, $\phi_{flat}$) whereas others differed ($n_{min}$, $k$, $\alpha$, $\beta$) (see Table 1), which suggests that G3Point GSD calibration may be needed in individual rivers with distinct grain sizes, grain shapes, or topographies.

Table 1. Accuracy of G3Point/Pro+ grain size ($b$), driving protrusion ($p_D$), resisting protrusion ($p_R$), and $\tau_c$ distributions in each experiment (narrow vs wide GSD). Two example G3Point $k$ values are shown for each experiment using the optimal G3Point input variable combination, which was assessed using p values and % errors for each output variable ($b$, $p_D$, $p_R$, and $\tau_c$).

| Experiment (example $k$ value) | p value | | | | % error in 10th, 50th, 90th percentiles | | | |
|---|---|---|---|---|---|---|---|---|
| | $b$ | $p_D$ | $p_R$ | $\tau_c$ | $b$ | $p_D$ | $p_R$ | $\tau_c$ |
| Narrow GSD ($k$=30) | 0.51 | 0.82 | 0.95 | 0.04 | 11, 4, 14 | 13, 5, <1 | 367[1], 5, <1 | 49, 20, 8 |
| Narrow GSD ($k$=40) | 0.20 | 0.97 | 0.91 | 0.002 | 17, 9, 8 | 11, 4, 3 | 354[1], <1, <1 | 61, 28, 19 |
| Wide GSD ($k$=10) | 0.03 | 0.89 | 0.48 | 0.66 | 3, 13, 18 | 2, 4, 11 | 7[1], 322[1], 23 | 48, 8, <1 |
| Wide GSD ($k$=15) | 0.15 | 0.82 | 0.69 | 0.002 | 20, 14, 9 | 4, 5, 5 | 7[1], 193[1], 13 | 115, 39, 51 |

[1] denotes that manual-based and/or G3Point/Pro+ $p_R$ estimates were negative and were converted to zero values in $\tau_c$ calculations. Optimized G3Point input variables for the narrow GSD ($n_{min}$=50, $C_F$=0.1, $\alpha$=10°, $\beta$=10°, $\phi_{flat}$=0.1) and wide GSD ($n_{min}$=10, $C_F$=0.1, $\alpha$=60°, $\beta$=20°, $\phi_{flat}$=0.1) experiments were used in Table 1 and Figures 4, 5a-d, and 6.

G3Point accurately identified the locations and approximate perimeters of many grains but sometimes lumped grains together or split grains into multiple particles, even using the optimal G3Point input variables (Figures 6 and 7). For the optimal G3Point input variables, $k$ altered the relative number of lumped or split grains but could not eliminate either problem (Figure 6b vs 6c; Figure 7b vs 7c). In the wide GSD experiment, G3Point also misidentified small particles

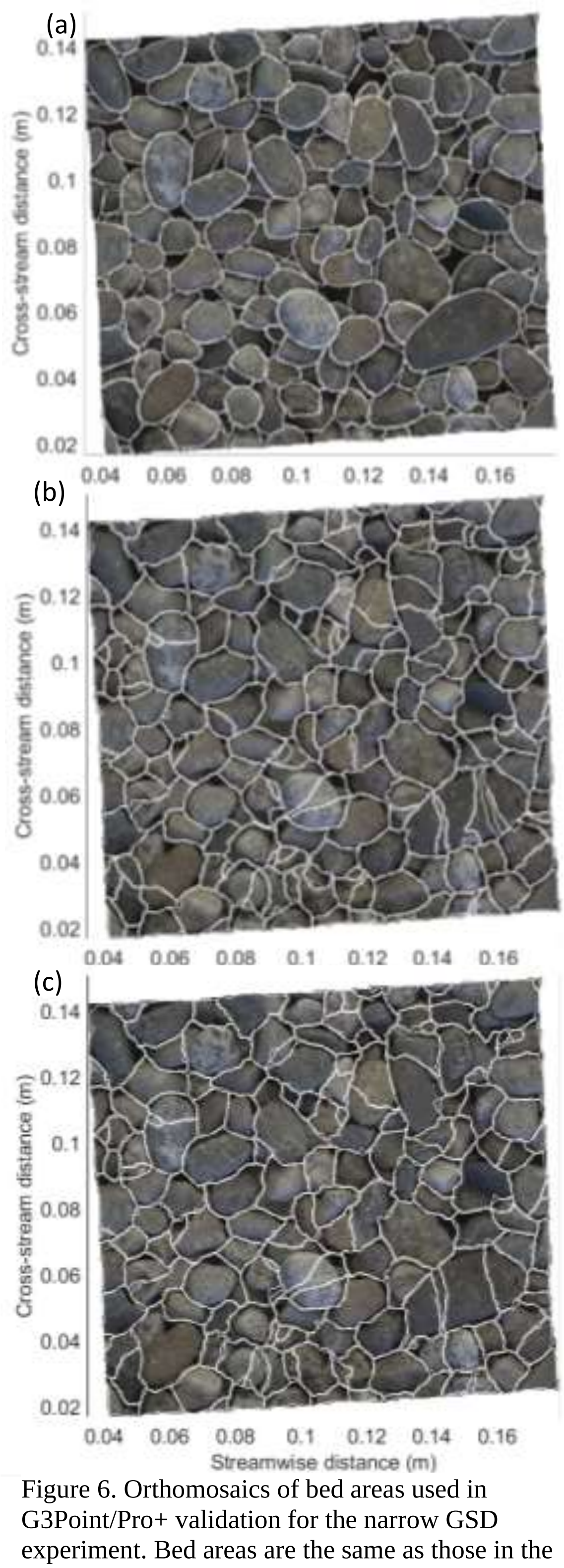


Figure 6. Orthomosaics of bed areas used in G3Point/Pro+ validation for the narrow GSD experiment. Bed areas are the same as those in the white boxes in Figure 1. White lines show (a) manual grain perimeters and (b-c) example grain perimeters from the optimal G3Point input variable combination (see Table 1) with a *k* value of (b) 30 and (c) 40.

sitting on top of large relatively flat grains (Figure 7). Other G3Point input variable combinations also produced reasonable GSD with low percent errors and high p values but had greater grain identification/perimeter errors than our optimal input variable values (Figure 7d).

### 3.3 Pro+ validation

We now use the range of G3Point *k* values and the optimal G3Point input variable combination from the last section in Pro+ to calculate $p_D$, $p_{R,}$ and $\tau_c$ distributions. For all tested *k* values, G3Point/Pro+ $p_D$ and $p_R$ distributions closely mimicked the shape of the manual-based protrusion distributions in each experiment (Figure 5b and 5e). This is further supported by relatively high p values for $p_D$ and $p_R$ in both experiments (Table 1), implying G3Point/Pro+ and manual-based protrusion distributions may not be statistically different within the distribution uncertainties. Although all percent errors for the G3Point/Pro+ $p_D$ distributions were low, percent errors for the 10$^{th}$ or 50$^{th}$

percentiles of the G3Point/Pro+ $p_R$ distribution were often large (Table 1). These percentiles had negative G3Point/Pro+ and/or manual-based protrusion values (see Figure 4a for example), which are automatically set to zero in the $\tau_c$ calculations (see supporting information). Therefore, some of the G3Point/Pro+ $p_R$ errors did not propagate to $\tau_c$.

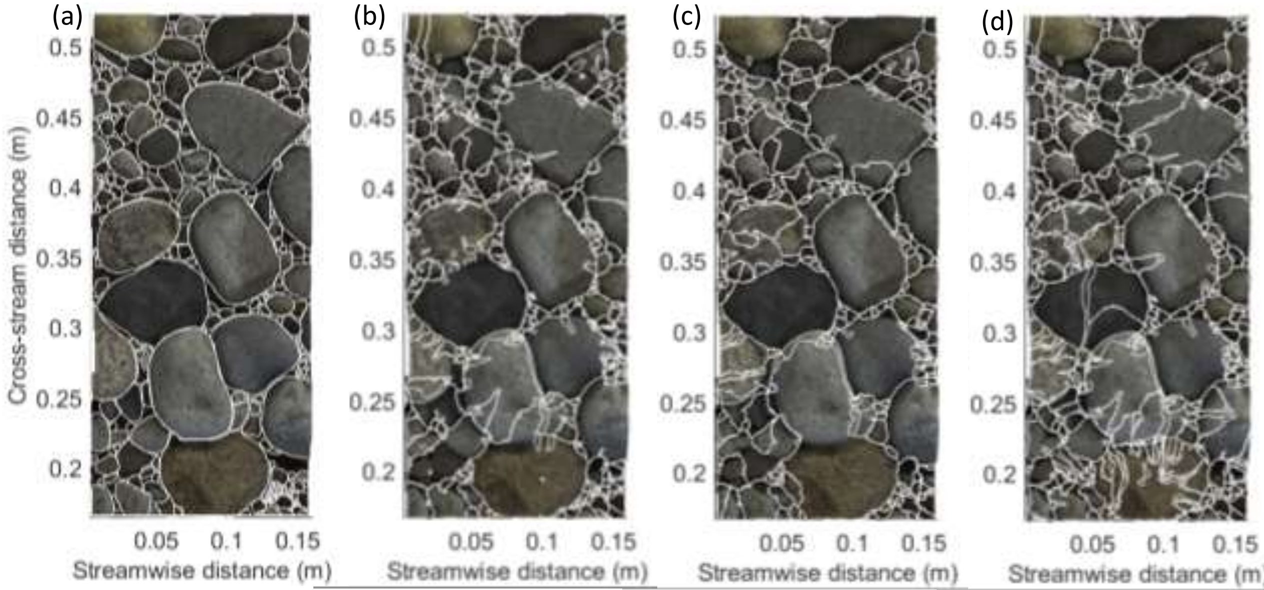


Figure 7. Orthomosaics of bed areas used in G3Point/Pro+ validation for the wide GSD experiments. Bed areas are the same as those in the white boxes in Figure 1. White lines show (a) manual grain perimeters example grain and (b-c) perimeters from the optimal G3Point input variable combination (see Table 1) with a *k* value of (b) 10 and (c) 15. (d) shows perimeters from a G3Point input variable combination ($n_{min}$=50, $C_F$=0.2, $\alpha$=60°, $\beta$=10°, $\phi_{flat}$=0.1) that produced reasonably accurate G3Point/Pro+ grain size, protrusion, and $\tau_c$ distributions.

The G3Point/Pro+ and manual-based $\tau_c$ distributions had similar shapes in the wide GSD experiment (Figure 5f) and some small shape discrepancies (e.g., use of a single *k* value cannot fully match the manual distribution) in the narrow GSD experiment (Figure 5c). In each experiment, these visually similar G3Point/Pro+ and manual-based $\tau_c$ distributions were only statistically similar within the distribution uncertainties (high p values) for some of the tested *k* values (Table 1). This implies that obtaining similar manual-based and G3Point/Pro+ $\tau_c$ distributions may be more difficult than obtaining similar grain size and protrusion distributions.

Indeed, the percent errors in the G3Point/Pro+ $\tau_c$ distributions also strongly depended on *k* and were relatively high compared to those for grain size and some protrusion percentiles (Table 1).

# 4 Discussion

## 4.1 Future work to test and improve Pro+

We used two laboratory experiments with different GSD and bed topographies to validate Pro+ sensitivity to input G3Point grain sizes and grain locations. Our results demonstrate that generally reasonable G3Point/Pro+ protrusion and $\tau_c$ distributions can be obtained by optimizing only the GSD in G3Point. G3Point/Pro+ $\tau_c$ generally had larger errors than G3Point/Pro+ protrusion or G3Point grain size because the $\tau_c$ equation nonlinearly combines $b$, $p_D$, and $p_R$ uncertainties. Some of the differences between G3Point and manual GSDs can be attributed to errors common to photogrammetry measurements (Buscombe et al., 2010; Buscombe and Masselink, 2009; Garefalakis et al., 2023; Graham, 2005) such as partly buried grains, difficulty in identifying the *b* axis in 2D images, and vertically angled *b* axes that cause over- or under-estimation of axis length. However, most errors were largely caused by G3Point misidentified grain boundaries and locations (Figures 6 and 7). In particular, reasonably accurate grain size and protrusion distributions could be obtained by G3Point input variable combinations that produced very inaccurate grain perimeters (Figure 7d). G3Point can obtain the correct GSD for the wrong reasons, and we recommend using a combination of quantitative GSD errors and qualitative visual grain perimeter assessment in validation and calibration of G3Point.

Instead of using G3Point, Pro+ also has the option of inputting a detrended point cloud (or DEM in the format of a detrended point cloud), grain sizes, and grain perimeter coordinates from other software. For example, deep learning can automatically identify grain perimeters and grain sizes in georeferenced orthomosaics from drone flights (Chen et al., 2020). Other methods based on point clouds or DEMs could also provide the necessary Pro+ inputs such as that of Wu et al. (2021), which uses factorial kriging to identify grain edges in DEMs. Butler et al. (2001) also uses a variety of methods employing orthophotographs, DEMs, watershed segmentation, and ellipsoidal fits to detect grain perimeters and sizes. Further Pro+ testing using such input software would be beneficial.

Beyond testing Pro+ sensitivity to input grain sizes and grain perimeters, comparisons are needed between Pro+ protrusion and $\tau_c$ distributions and those from direct measurements. For example, Hodge et al (in review) compared Pro+ protrusion values to those measured using a ruler in the field and those measured using 3D CT scan data. All tested methods produced similar normalized protrusion (protrusion/grain size) values in each of eight different sediment patches. However, the pattern of normalized protrusion between the patches was not consistent for the different methods, suggesting that different protrusion methods/definitions may complicate validation of Pro+.

For $\tau_c^*$, such comparisons are further complicated because Pro+ provides a $\tau_c^*$, $\tau_{ci}^*$, and/or $\tau_{c50}^*$ distribution whereas most direct estimates only have one value. A low percentile (e.g., 1-10) of the calculated $\tau_{ci}^*$ or $\tau_{c50}^*$ distribution is often recommended because it corresponds to easily mobile grains that would be measured in bedload samplers or through particle motions (Buffington et al., 1992; Buxton et al., 2015; Kirchner et al., 1990). The exact percentile could be informed by future research comparing Pro+ $\tau_{ci}^*$ or $\tau_{c50}^*$ distributions to directly measured values. Encouragingly, force-balance equations can provide $\tau_c^*$ within the range of values determined using reference transport or flow competence approaches (Buffington et al., 1992; Hodge et al., 2013, 2020; Kirchner et al., 1990; Lamb et al., 2008; Wiberg and Smith, 1987). However, different $\tau_c^*$ values even occur between the direct reference transport rate and competence methods; each method involves a unique set of uncertainties and limitations that will also complicate Pro+ comparisons (Buffington and Montgomery, 1997; Smith et al., 2023; Wilcock, 1993).

In addition to further Pro+ validation, future research could focus on better characterizing protrusion and the flow field needed for $\tau_c^*$ calculations. We used two representative surrounding bed elevation percentiles, $10^{th}$ for $p_D$ and $50^{th}$ for $p_R$, to capture the different impacts of protrusion on driving and resisting forces, respectively. Previous studies often only use the median (or higher) surrounding bed elevation that may result in many negative protrusion values for which calculated flow velocities and driving forces are zero. Particles below the median bed elevation can actually experience positive time-averaged flow velocities because of the complex flow and pressure field driven by sheltering obstacles. Particles with zero protrusion also could have higher lift forces than those that protrude high into the flow column (Schmeeckle et al., 2007). Although spatially averaged sheltering effects are partly and indirectly included in the velocity profile for the roughness layer (Lamb et al., 2017b), the local flow fields that cause measurable drag and lift forces for very low or negative protrusion grains are not included in simple force balances. More studies are needed that measure/model the complex near-bed flow field over the rough topographies typical of gravel bedded rivers (Curran and Tan, 2014; Lacey and Roy, 2007; Monsalve et al., 2017; Strom and Papanicolaou, 2007). Such information could be used to improve the flow equations employed in Pro+.

### 4.2 Potential Pro+ calculations for each grain size

The protrusion and $\tau_c$ distributions for the entire bed in Figure 5 obscure that each grain size bin has unique distributions of these variables. We cannot assess the accuracy of G3Point/Pro+ protrusion and $\tau_c$ distributions for each grain size bin because we used small bed areas in our manual measurements, which resulted in a low number of sampled grains in each bin. As an example application of G3Point/Pro+, we show the $p_D$ distribution in the wide GSD experiment for one grain size bin (4 mm) that potentially had enough manually sampled particles (51) to define a distribution. The optimized G3Point input variable combination for this experiment (Table 1) also provided a G3Point/Pro+ $p_D$ distribution that generally matched the manual-based

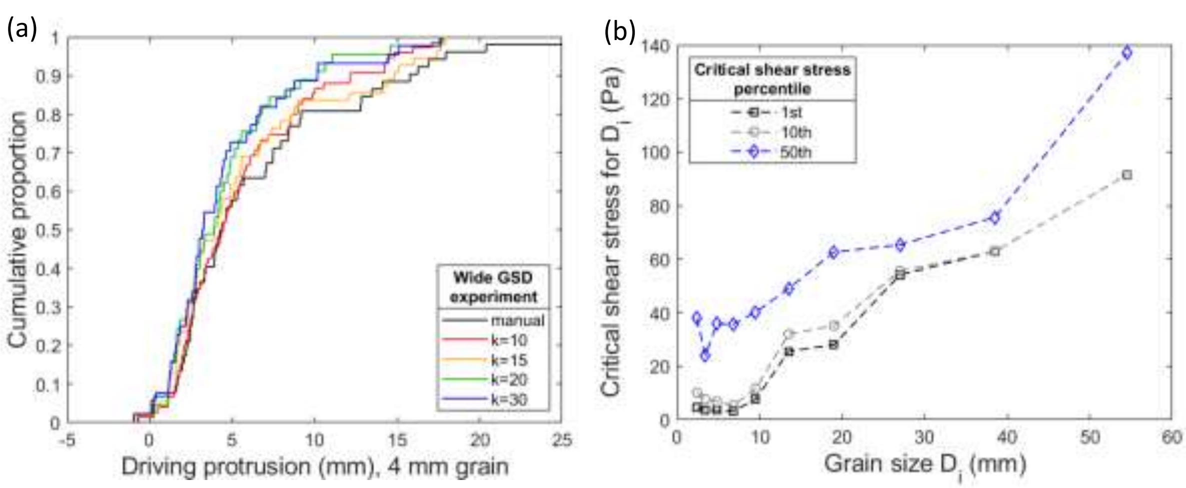


Figure 8. Example using G3Point/Pro+ to obtain protrusion and $\tau_{ci}$ for each grain size bin. (a) Manual-based (black line) and G3Point/ Pro+ (colored lines labeled with *k* values) driving protrusion distributions for the 4 mm grain size bin in the wide GSD experiment. (b) Example G3Point/Pro+ calculated (with *k*=10) $\tau_{ci}$ distribution percentiles ($1^{st}$, $10^{th}$, $50^{th}$) for each grain size bin in the wide GSD experiment. The optimal G3Point input variables for the wide GSD experiment (see Table 1) were used in all calculations.

distribution for the 4 mm grain size bin (Figure 8a). Calibrated G3Point inputs to Pro+ may also allow for accurate G3Point/Pro+ protrusion estimates for a given grain size ($D_i$) of interest.

With a greater number of particles and therefore protrusion measurements in each grain size bin, Pro+ can similarly estimate the $\tau_{ci}$ distribution for each $D_i$, which are used in hiding functions. Although we lack the proper sample size to develop hiding functions, we tested if $\tau_{ci}$ increases with $D_i$, which is commonly expected unless hiding effects perfectly balance grain weight effects to produce equal mobility onset of motion conditions. We used low example percentiles (1st, 10th and 50th) of the $\tau_{ci}$ distributions to represent particles that are easily mobile. These $\tau_{ci}$ percentiles generally increased with larger $D_i$ (Figure 8b), suggesting Pro+ could create hiding functions after further testing.

### 4.3 Pro+ applicability and input considerations

Several limitations need to be considered before applying Pro+ to a wide range of river systems. Obtaining the representative bed point cloud or DEM (converted to a point cloud format) is key for accurate Pro+ estimates. The representative bed area to sample (e.g., 1 x 1 m) depends on 1) whether only $\tau_{c50}^*$ or $\tau_{ci}^*$ for all grain sizes is needed, 2) the area needed to obtain a representative grain size sample, and 3) the area needed to accurately determine $k_s$ and protrusion, which are functions of either the $D_{84}$ or $\sigma_z$. We hypothesize that G3Point/deep learning/Pro+ estimated $D_{50}$ and $\tau_{c50}^*$ could require a sample size of grains similar to that used for pebble counts. If $\tau_{ci}^*$ for all grain sizes is desired, then a larger sample size and therefore bed area is required to ensure proper sampling in all grain size bins. The distance over which protrusion and $k_s$ must be measured is still an open research area, although our results and those of Smith et al. (2023) suggest that protrusion may be relatively insensitive to search distance. If bedform roughness is present, care must be taken in detrending bed elevations and in the distance over which $k_s$ is measured to properly include the effects of bedforms on flow roughness (see details in Bertin et al., 2017; Powell et al., 2016).

The streambed point cloud could be obtained through photographs coupled with SfM photogrammetry, ground-based LiDAR, or possibly the new iPhone LiDAR if resolution improves (Monsalve et al., 2023). All of these methods generally require an unsubmerged bed and/or submersible cameras to eliminate potential water distortion and reflection effects. Calculations to remove these water effects (Partama et al., 2018; Zhang et al., 2022) may also allow for Pro+ application on submerged beds. For coupled G3Point/Pro+ application to gravel-bedded rivers, G3Point needs calibration with some measured GSD for Pro+ to provide generally accurate protrusion and $\tau_c$ distributions. If the point cloud for G3Point/Pro+ is from photographs and SfM, the calibrating GSD could be manually measured on a scaled orthomosaic as performed here. This would eliminate some of the uncertainties in G3Point calibration that arise from different GSD sampling methods (Steer et al., 2022).

Although we tested G3Point and Pro+ using grain sizes as small as 2 mm, G3Point cannot provide accurate GSD for beds with a large proportion of sand (see discussion in Steer et al., 2022). Sand content also influences $\tau_c^*$ for gravel (Wilcock and Crowe, 2003) by potentially altering $k_s$ (Venditti et al., 2010), $\phi_p$, or $\phi_f$. But the variation of these three Pro+ inputs with bed sand content is uncertain. Given these uncertainties, we do not recommend using Pro+ on beds with significant surface sand contents.

In addition to grain size considerations, Pro+ also requires numerous input variables for protrusion and $\tau_c^*$ calculations, which are discussed in detail in the methods and supporting information. In particular, the mean and standard deviation of $\phi_f$ can strongly influence calculated resisting forces and $\tau_c^*$ values (Yager et al., 2018a). These $\phi_f$ values can be informed by those in Yager et al (2018a) or by resisting force measurements using a load cell in the same bed area after topographic data collection. The input mean and standard deviation of $\phi_f$ can be adjusted until the load cell and output Pro+ resisting force distributions match. Future studies could develop correlations between measured resisting forces and bed structural components estimated from point clouds such as imbrication, interlocking, and clustering (Aberle and Nikora, 2006; Curran and Waters, 2014; Hodge et al., 2009; Mao, 2012; Ockelford and Haynes, 2013; Wu et al., 2018). Such correlations could then be included in Pro+ to estimate $\phi_f$ values only from point clouds.

### 4.4 Application of Pro+ to predict and understand $\tau_c^*$

Pro+ can provide informed estimates of $\tau_{c50}^*$ and hiding function exponents in many gravel-bedded rivers using the actual bed conditions (i.e., protrusion, grain size, roughness) and some of the mechanics (e.g., applied and resisting forces) of sediment motion. These Pro+ estimates could replace the often arbitrary and subjective choices of $\tau_{c50}^*$ and hiding function exponents from the wide range of values in the literature (Buffington and Montgomery, 1997). We expect that such informed estimates of $\tau_{c50}^*$ would improve sediment transport, channel stability, and onset of motion predictions.

In addition to potentially supplying a single representative $\tau_{ci}^*$ value, Pro+ also provides a distribution of $\tau_{ci}^*$ for a given grain size because of different particle arrangements and local flow conditions. In calculations of bedload transport, shear stress distributions are usually ignored in favor of single values of $\tau_{ci}^*$ and reach-averaged applied shear stresses. Use of applied shear stress distributions and $\tau_{ci}^*$ distributions in bedload transport equations can reduce errors in predicted sediment fluxes compared to using single values of these shear stresses (Ferguson, 2003; Monsalve et al., 2016; Segura and Pitlick, 2015; Yager et al., 2018b; Yager and Schmeeckle, 2013). When possible, we recommend using the entire Pro+ $\tau_{ci}^*$ distribution that could be coupled with reach-scale or patch-scale shear stress distributions from 2D hydraulic models following the methods outlined in Monsalve et al. (2016) and Segura and Pitlick (2015).

Pro+ could also be used to mechanistically explain some of the observed $\tau_{c50}^*$ variability between rivers. Protrusion is a dominant control on driving forces, resisting forces, and $\tau_c^*$ (Hodge et al., 2020; Kirchner et al., 1990; Schmeeckle et al., 2007; Smith et al., 2023; Xie et al., 2023; Yager et al., 2018a) and Pro+ explicitly includes these effects. Similarly, Pro+ could be used to explain the large measured variability in hiding function exponents, which are likely partly controlled by bed GSD (Shvidchenko et al., 2001) and protrusion. Finally, Pro+ could estimate temporal changes in $\tau_c^*$ given the potential influence of protrusion on $\tau_c^*$ variations with time (Masteller and Finnegan, 2017).

## 5. Conclusions

Critical Shields stresses for the onset of sediment transport have considerable uncertainty but can have large impacts on channel stability and sediment transport calculations. To address this problem, we developed a mechanistic-based method called Pro+ that builds upon existing software that calculates grain sizes from bed point clouds. When coupled with grain size estimating software, Pro+ can determine particle protrusion and $\tau_c^*$ distributions as well as hiding functions in gravel bedded rivers. Care must be taken that the grain estimating software correctly identifies grain boundaries and grain locations, which were a large potential source of error in protrusion and $\tau_c^*$ calculations. Pro+ obtained $\tau_c^*$ distributions can provide informed estimates of the onset of motion rather than an arbitrarily chosen $\tau_c^*$ value from the wide range of scatter observed in gravel-bedded rivers.

## References


Aberle J, Nikora V. 2006. Statistical properties of armored gravel bed surfaces. Water Resources Research **42** : W11414. DOI: 10.1029/2005WR004674

Aberle J, Smart GM. 2003. The influence of roughness structure on flow resistance on steep slopes. Journal of Hydraulic Research **41** : 259–269. DOI: 10.1080/00221680309499971

Bathurst JC. 2013. Critical conditions for particle motion in coarse bed materials of nonuniform size distribution. Geomorphology **197** : 170–184. DOI: 10.1016/j.geomorph.2013.05.008

Bertin S, Groom J, Friedrich H. 2017. Isolating roughness scales of gravel-bed patches. Water Resources Research **53** : 6841–6856. DOI: 10.1002/2016WR020205

Bi D, Zhang J, Chakraborty B, Behringer RP. 2011. Jamming by shear. Nature **480** : 355–358. DOI: 10.1038/nature10667

Budwig R, Goodwin P. 2012. Ecohydraulics Research Mountain StreamLab - a facility for collaborative research and education. In Innovations 2012: world innovations in engineering education and research (eds. Aung, W., Ilic, V., Mertanen, O., Moscinski, J. & Uhomoibh, J.) , . 17–28.

Buffington JM, Dietrich WE, Kirchner JW. 1992. Friction Angle Measurements on a Naturally Formed Gravel Streambed: Implications for Critical Boundary Shear Stress. Water Resources Research **28** : 411–425.

Buffington JM, Montgomery DR. 1997. A systematic analysis of eight decades of incipient motion studies, with special reference to gravel-bedded rivers. Water Resources Research **33** : 1993–2029.

Buscombe D, Masselink G. 2009. Grain-size information from the statistical properties of digital images of sediment. Sedimentology **56** : 421–438. DOI: 10.1111/j.1365-3091.2008.00977.x

Buscombe D, Rubin DM, Warrick JA. 2010. A universal approximation of grain size from images of noncohesive sediment. Journal of Geophysical Research: Earth Surface **115** : F02015. DOI: 10.1029/2009JF001477

Butler JB, Lane SN, Chandler JH. 2001. Automated extraction of grain-size data from gravel surfaces using digital image processing. Journal of Hydraulic Research **39** : 519–529. DOI: 10.1080/00221686.2001.9628276

Buxton TH, Buffington JM, Yager EM, Hassan MA, Fremier AK. 2015. The relative stability of salmon redds and unspawned streambeds. Water Resources Research : 6074–6092. DOI: 10.1002/2015WR016908

Charru F, Mouilleron H, Eiff O. 2004. Erosion and deposition of particles on a bed sheared by a viscous flow. Journal of Fluid Mechanics **519** : 55–80. DOI: 10.1017/S0022112004001028

Chen Z, Scott TR, Bearman S, Anand H, Keating D, Scott C, Arrowsmith JR, Das J. 2020. Geomorphological Analysis Using Unpiloted Aircraft Systems, Structure from Motion, and Deep Learning. presented at the 2020 IEEE/RSJ International Conference on Intelligent Robots and Systems (IROS). Las Vegas, NV, USA. 1276–1283 pp. 24 October [online] Available from: https://ieeexplore.ieee.org/document/9341354/ (Accessed 26 March 2023)

Cúñez FD, Franklin EM, Houssais M, Arratia P, Jerolmack DJ. 2022. Strain hardening by sediment transport. Physical Review Research **4** : L022055. DOI: 10.1103/PhysRevResearch.4.L022055

Curran JC, Tan L. 2014. The effect of cluster morphology on the turbulent flows over an armored gravel bed surface. Journal of Hydro-environment Research **8** : 129–142. DOI: 10.1016/j.jher.2013.11.002

Curran JC, Waters KA. 2014. The importance of bed sediment sand content for the structure of a static armor layer in a gravel bed river. Journal of Geophysical Research: Earth Surface **119** : 1484–1497. DOI: 10.1002/2014JF003143

Daniels KE, Kollmer JE, Puckett JG. 2017. Photoelastic force measurements in granular materials. Review of Scientific Instruments **88** : 051808. DOI: 10.1063/1.4983049

Duffin J, Yager EM, Buffington JM, Benjankar R, Borden C, Tonina D. 2023. Impact of flow regulation on stream morphology and habitat quality distribution. Science of The Total Environment **878** : 163016. DOI: 10.1016/j.scitotenv.2023.163016

Fenton JD, Abbott JE. 1977. Initial Movement of Grains on a Stream Bed: The Effect of Relative Protrusion. Proceedings of the Royal Society A: Mathematical, Physical and Engineering Sciences **352** : 523–537. DOI: 10.1098/rspa.1977.0014

Ferguson R. 2003. The missing dimension: effects of lateral variation on 1-D calculations of fluvial bedload transport. Geomorphology **56** : 1–14. DOI: 10.1016/S0169-555X(03)00042-4

Ferguson RI, Hardy RJ, Hodge RA. 2019. Flow resistance and hydraulic geometry in bedrock rivers with multiple roughness length scales. Earth Surface Processes and Landforms **44** : 2437–2449. DOI: 10.1002/esp.4673

Garcia M (ed). 2008. Sedimentation Engineering: Processes, Measurements, Modeling, and Practice . 110th ed. American Society of Civil Engineers: Reston, VA [online] Available from: https://ascelibrary.org/doi/book/10.1061/9780784408148 (Accessed 11 April 2023)

Garefalakis P, Do Prado AH, Mair D, Douillet GA, Nyffenegger F, Schlunegger F. 2023. Comparison of three grain size measuring methods applied to coarse-grained gravel deposits. Sedimentary Geology **446** : 106340. DOI: 10.1016/j.sedgeo.2023.106340

Graham DJ. 2005. A transferable method for the automated grain sizing of river gravels. Water Resources Research **41** DOI: 10.1029/2004WR003868 [online] Available from: http://www.agu.org/pubs/crossref/2005/2004WR003868.shtml

Haynes H, Pender G. 2007. Stress History Effects on Graded Bed Stability. Journal of Hydraulic Engineering **133** : 343–349. DOI: 10.1061/(ASCE)0733-9429(2007)133:4(343)

Heald J, McEwan I, Tait S. 2004. Sediment transport over a flat bed in a unidirectional flow: simulations and validation. Richards K and Dove M (eds). Philosophical Transactions of the Royal Society of London. Series A: Mathematical, Physical and Engineering Sciences **362** : 1973–1986. DOI: 10.1098/rsta.2004.1426

Hodge R, Brasington J, Richards K. 2009. Analysing laser-scanned digital terrain models of gravel bed surfaces: linking morphology to sediment transport processes and hydraulics. Sedimentology **56** : 2024–2043. DOI: 10.1111/j.1365-3091.2009.01068.x

Hodge RA, Buechel MEH. 2022. The influence of bedrock river morphology and alluvial cover on gravel entrainment. Part 2: Modelling critical shear stress. Earth Surface Processes and Landforms **47** : 3348–3360. DOI: 10.1002/esp.5462

Hodge RA, Sear DA, Leyland J. 2013. Spatial variations in surface sediment structure in riffle-pool sequences: a preliminary test of the Differential Sediment Entrainment Hypothesis (DSEH). Earth Surface Processes and Landforms **38** : 449–465. DOI: 10.1002/esp.3290

Hodge RA, Voepel H, Leyland J, Sear DA, Ahmed S. 2020. X-ray computed tomography reveals that grain protrusion controls critical shear stress for entrainment of fluvial gravels. Geology **48** : 149–153. DOI: 10.1130/G46883.1

Hodge RA, Voepel H, Yager EM, Leyland J, Johnson JPL, Sear DA, Ahmed S. in review. Improving predictions of critical shear stress in gravel bed rivers: identifying the onset of sediment transport and quantifying sediment structure. Earth Surface Processes and Landforms

Johnson JPL. 2014. A surface roughness model for predicting alluvial cover and bed load transport rate in bedrock channels: Bedrock roughness alluvial cover model. Journal of Geophysical Research: Earth Surface **119** : 2147–2173. DOI: 10.1002/2013JF003000

Johnson JPL. 2016. Gravel threshold of motion: a state function of sediment transport disequilibrium? Earth Surface Dynamics **4** : 685–703. DOI: 10.5194/esurf-4-685-2016

Johnson JPL. 2017. Clustering statistics, roughness feedbacks, and randomness in experimental step-pool morphodynamics. Geophysical Research Letters **44** : 3653–3662. DOI: 10.1002/2016GL072246

Kirchner JW, Dietrich WE, Iseya F, Ikeda H. 1990. The variability of critical shear stress, friction angle, and grain protrusion in water-worked sediments. Sedimentology **37** : 647–672.

Lacey RWJ, Roy AG. 2007. A comparative study of the turbulent flow field with and without a pebble cluster in a gravel bed river: TECHNICAL NOTE. Water Resources Research **43** DOI: 10.1029/2006WR005027 [online] Available from: http://doi.wiley.com/10.1029/2006WR005027 (Accessed 25 April 2023)

Lamb MP, Brun F, Fuller BM. 2017a. Direct measurements of lift and drag on shallowly submerged cobbles in steep streams: Implications for flow resistance and sediment transport. Water Resources Research **53** : 7607–7629. DOI: 10.1002/2017WR020883

Lamb MP, Brun F, Fuller BM. 2017b. Hydrodynamics of steep streams with planar coarse-grained beds: Turbulence, flow resistance, and implications for sediment transport. Water Resources Research **53** : 2240–2263. DOI: 10.1002/2016WR019579

Lamb MP, Dietrich WE, Venditti JG. 2008. Is the critical Shields stress for incipient sediment motion dependent on channel-bed slope? Journal of Geophysical Research **113** DOI: 10.1029/2007JF000831 [online] Available from: http://www.agu.org/pubs/crossref/2008/2007JF000831.shtml (Accessed 3 December 2011)

Luo M, Jiang Y, Wang S, Liu X, Huang E. 2023. The effect of stress history on fluctuation of bedload transport rate and bed topography in gravel-bed streams. Journal of Hydrology **616** : 128732. DOI: 10.1016/j.jhydrol.2022.128732

Mao L. 2012. The effect of hydrographs on bed load transport and bed sediment spatial arrangement. Journal of Geophysical Research **117** : F03024. DOI: 10.1029/2012JF002428

Masteller CC, Finnegan NJ. 2017. Interplay between grain protrusion and sediment entrainment in an experimental flume. Journal of Geophysical Research: Earth Surface **122** : 274–289. DOI: 10.1002/2016JF003943

Masteller CC, Finnegan NJ, Turowski JM, Yager EM, Rickenmann D. 2019. History-Dependent Threshold for Motion Revealed by Continuous Bedload Transport Measurements in a Steep Mountain Stream. Geophysical Research Letters DOI: 10.1029/2018GL081325 [online] Available from: http://doi.wiley.com/10.1029/2018GL081325 (Accessed 21 March 2019)

Monsalve A, Yager EM, Schmeeckle MW. 2017. Effects of Bed Forms and Large Protruding Grains on Near-Bed Flow Hydraulics in Low Relative Submergence Conditions. Journal of Geophysical Research: Earth Surface DOI: 10.1002/2016JF004152 [online] Available from: http://doi.wiley.com/10.1002/2016JF004152 (Accessed 13 November 2017)

Monsalve A, Yager EM, Tonina D. 2023. Evaluating Apple iPhone LiDAR measurements of topography and roughness elements in coarse bedded streams. Journal of Ecohydraulics : 1–11. DOI: 10.1080/24705357.2023.2204087

Monsalve A, Yager EM, Turowski JM, Rickenmann D. 2016. A probabilistic formulation of bed load transport to include spatial variability of flow and surface grain size distributions. Water Resources Research **52** : 3579–3598. DOI: 10.1002/2015WR017694

Ockelford A, Woodcock S, Haynes H. 2019. The impact of inter-flood duration on non-cohesive sediment bed stability. Earth Surface Processes and Landforms **44** : 2861–2871. DOI: 10.1002/esp.4713

Ockelford A-M, Haynes H. 2013. The impact of stress history on bed structure. Earth Surface Processes and Landforms **38** : 717–727. DOI: 10.1002/esp.3348

Partama IGY, Kanno A, Ueda M, Akamatsu Y, Inui R, Sekine M, Yamamoto K, Imai T, Higuchi T. 2018. Removal of water-surface reflection effects with a temporal minimum filter for UAV-based shallow-water photogrammetry: Removal of Water-Surface Reflection Effects for UAV-Photogrammetry. Earth Surface Processes and Landforms **43** : 2673–2682. DOI: 10.1002/esp.4399

Powell DM, Ockelford A, Rice SP, Hillier JK, Nguyen T, Reid I, Tate NJ, Ackerley D. 2016. Structural properties of mobile armors formed at different flow strengths in gravel-bed rivers: Mobile Armor Structure. Journal of Geophysical Research: Earth Surface **121** : 1494–1515. DOI: 10.1002/2015JF003794

Pretzlav KLG, Johnson JPL, Bradley DN. 2020. Smartrock Transport in a Mountain Stream: Bedload Hysteresis and Changing Thresholds of Motion. Water Resources Research **56** DOI: 10.1029/2020WR028150 [online] Available from: https://onlinelibrary.wiley.com/doi/10.1029/2020WR028150 (Accessed 30 January 2023)

Recking A. 2009. Theoretical development on the effects of changing flow hydraulics on incipient bed load motion. Water Resources Research **45** : W04401. DOI: 10.1029/2008WR006826

Rickenmann D. 2020. Effect of Sediment Supply on Cyclic Fluctuations of the Disequilibrium Ratio and Threshold Transport Discharge, Inferred From Bedload Transport Measurements Over 27 Years at the Swiss Erlenbach Stream. Water Resources Research **56** DOI: 10.1029/2020WR027741 [online] Available from: https://onlinelibrary.wiley.com/doi/10.1029/2020WR027741 (Accessed 30 January 2023)

Sanguinito S, Johnson J. 2012. Quantifying gravel overlap and dislodgement forces on natural river bars: implications for particle entrainment. Earth Surface Processes and Landforms **37** : 134–141. DOI: 10.1002/esp.2237

Schmeeckle MW, Nelson JM. 2003. Direct numerical simulation of bedload transport using a local, dynamic boundary condition. Sedimentology **50** : 279–301. DOI: 10.1046/j.1365-3091.2003.00555.x

Schmeeckle MW, Nelson JM, Shreve RL. 2007. Forces on stationary particles in near-bed turbulent flows. Journal of Geophysical Research **112** : F02003. DOI: 10.1029/2006JF000536

Schneider JM, Rickenmann D, Turowski JM, Kirchner JW. 2015. Self-adjustment of stream bed roughness and flow velocity in a steep mountain channel. Water Resources Research **51** : 7838–7859. DOI: 10.1002/2015WR016934

Segura C, Pitlick J. 2015. Coupling fluvial-hydraulic models to predict gravel transport in spatially variable flows. Journal of Geophysical Research: Earth Surface **120** : 834–855. DOI: 10.1002/2014JF003302

Shields IA. 1936. Anwendung der ahnlichkeitmechanik und der turbulenzforschung auf die gescheibebewegung . Berlin, Germany

Shvidchenko AB, Pender G, Hoey TB. 2001. Critical shear stress for incipient motion of sand/gravel streambeds. Water Resources Research **37**

Smart GM, Duncan MJ, Walsh JM. 2002. Relatively Rough Flow Resistance Equations. Journal of Hydraulic Engineering **128** : 568–578. DOI: 10.1061/(ASCE)0733-9429(2002)128:6(568)

Smith HEJ, Monsalve AD, Turowski JM, Rickenmann D, Yager EM. 2023. Controls of local grain size distribution, bed structure, and flow conditions on sediment mobility. Earth Surface Processes and Landforms : esp.5599. DOI: 10.1002/esp.5599

Steer P, Guerit L, Lague D, Crave A, Gourdon A. 2022. Size, shape and orientation matter: fast and automatic measurement of grain geometries from 3D point clouds . preprint. Cross-cutting themes: Digital Landscapes: Insights into geomorphological processes from high-resolution topography and quantitative interrogation of topographic data [online] Available from: https://egusphere.copernicus.org/preprints/2022/egusphere-2022-75/ (Accessed 30 January 2023)

Strom KB, Papanicolaou AN. 2007. ADV Measurements around a Cluster Microform in a Shallow Mountain Stream. Journal of Hydraulic Engineering **133** : 1379–1389. DOI: 10.1061/(ASCE)0733-9429(2007)133:12(1379)

Turowski JM, Badoux A, Rickenmann D. 2011. Start and end of bedload transport in gravel-bed streams. Geophysical Research Letters **38** : L04401. DOI: 10.1029/2010GL046558

Venditti JG, Dietrich WE, Nelson PA, Wydzga MA, Fadde J, Sklar L. 2010. Effect of sediment pulse grain size on sediment transport rates and bed mobility in gravel bed rivers. Journal of Geophysical Research **115** DOI: 10.1029/2009JF001418 [online] Available from: http://doi.wiley.com/10.1029/2009JF001418 (Accessed 23 May 2014)

Voepel H, Leyland J, Hodge RA, Ahmed S, Sear D. 2019. Development of a vector-based 3D grain entrainment model with application to X-ray computed tomography scanned riverbed sediment. Earth Surface Processes and Landforms **44** : 3057–3077. DOI: 10.1002/esp.4608

Walicka A, Pfeifer N, Borkowski A, Jóźków G. 2021. An automatic method for the measurement of coarse particle movement in a mountain riverbed. Measurement **174** : 109029. DOI: 10.1016/j.measurement.2021.109029

Wiberg PL, Smith JD. 1987. Calculations of the Critical Shear Stress for Motion of Uniform and Heterogeneous Sediments. Water Resources Research **23** : 1471–1480.

Wilcock PR. 1993. Critical Shear Stress of Natural Sediments. Journal of Hydraulic Engineering **119**

Wilcock PR, Crowe JC. 2003. Surface-based Transport Model for Mixed-Size Sediment. Journal of Hydraulic Engineering **129** : 120. DOI: 10.1061/(ASCE)0733-9429(2003)129:2(120)

Wu F-C, Wang C-K, Huang G-H. 2018. Delineation of gravel-bed clusters via factorial kriging. Geomorphology **308** : 161–174. DOI: 10.1016/j.geomorph.2018.02.013

Wu F-C, Wang C-K, Lo HP. 2021. FKgrain: A topography-based software tool for grain segmentation and sizing using factorial kriging. Earth Science Informatics **14** : 2411–2421. DOI: 10.1007/s12145-021-00660-z

Xie Y, Melville BW, Shamseldin AY, Whittaker CN, Yang Y. 2023. Direct measurement of the inertial drag and lift forces on entrained coarse particles at various protrusion heights. Earth Surface Processes and Landforms **48** : 371–385. DOI: 10.1002/esp.5491

Yager EM, Dietrich WE, Kirchner JW, McArdell BW. 2012. Prediction of sediment transport in step-pool channels. Water Resources Research **48** DOI: 10.1029/2011WR010829 [online] Available from: http://www.agu.org/pubs/crossref/2012/2011WR010829.shtml (Accessed 4 June 2012)

Yager EM, Schmeeckle MW. 2013. The influence of vegetation on turbulence and bed load transport. Journal of Geophysical Research: Earth Surface **118** : 1585–1601. DOI: 10.1002/jgrf.20085

Yager EM, Schmeeckle MW, Badoux A. 2018a. Resistance Is Not Futile: Grain Resistance Controls on Observed Critical Shields Stress Variations. Journal of Geophysical Research: Earth Surface DOI: 10.1029/2018JF004817 [online] Available from: https://onlinelibrary.wiley.com/doi/abs/10.1029/2018JF004817 (Accessed 3 January 2019)

Yager EM, Venditti JG, Smith HJ, Schmeeckle MW. 2018b. The trouble with shear stress. Geomorphology **323** : 41–50. DOI: 10.1016/j.geomorph.2018.09.008

Yochum SE, Bledsoe BP, David GCL, Wohl E. 2012. Velocity prediction in high-gradient channels. Journal of Hydrology **424–425** : 84–98. DOI: 10.1016/j.jhydrol.2011.12.031

Zhang C, Sun A, Hassan MA, Qin C. 2022. Assessing Through-Water Structure-from-Motion Photogrammetry in Gravel-Bed Rivers under Controlled Conditions. Remote Sensing **14** : 5351. DOI: 10.3390/rs14215351